Antenna-coupled infrared nanospectroscopy of intramolecular vibrational interaction

Roland Wilcken[a,1] (iD), Jun Nishida[a] (iD), Johan F. Triana[b] (iD), Aurelian John-Herpin[c], Hatice Altug[c] (iD), Sandeep Sharma[d] (iD), Felipe Herrera[b,e,1] (iD), and Markus B. Raschke[a,1] (iD)

Many photonic and electronic molecular properties, as well as chemical and biochemical reactivities are controlled by fast intramolecular vibrational energy redistribution (IVR). This fundamental ultrafast process limits coherence time in applications from photochemistry to single quantum level control. While time-resolved multidimensional IR-spectroscopy can resolve the underlying vibrational interaction dynamics, as a nonlinear optical technique it has been challenging to extend its sensitivity to probe small molecular ensembles, achieve nanoscale spatial resolution, and control intramolecular dynamics. Here, we demonstrate a concept how mode-selective coupling of vibrational resonances to IR nanoantennas can reveal intramolecular vibrational energy transfer. In time-resolved infrared vibrational nanospectroscopy, we measure the Purcell-enhanced decrease of vibrational lifetimes of molecular vibrations while tuning the IR nanoantenna across coupled vibrations. At the example of a Re-carbonyl complex monolayer, we derive an IVR rate of (25 ± 8) cm^{-1} corresponding to (450 ± 150) fs, as is typical for the fast initial equilibration between symmetric and antisymmetric carbonyl vibrations. We model the enhancement of the cross-vibrational relaxation based on intrinsic intramolecular coupling and extrinsic antenna-enhanced vibrational energy relaxation. The model further suggests an anti-Purcell effect based on antenna and laser–field–driven vibrational mode interference which can counteract IVR-induced relaxation. Nanooptical spectroscopy of antenna-coupled vibrational dynamics thus provides for an approach to probe intramolecular vibrational dynamics with a perspective for vibrational coherent control of small molecular ensembles.

nanospectroscopy | intramolecular vibrational redistribution | light–matter interaction

Many functional molecular properties are controlled by fast intramolecular relaxation intrinsic to the coupled many-body environment in polyatomic molecules. In particular, intramolecular vibrational energy redistribution (IVR) describes the vibrational energy relaxation into the vibrational manifold within a molecule representing its own heat bath (1–8). This process is vital for all chemical processes from unimolecular (9–12) to enzymatic reactions (6). Due to the anharmonic coupling between the large number of vibrational modes even in small molecules, IVR typically occurs on few picosecond timescales. This limits the lifetime and coherence of an excited vibrational state, which would otherwise have lifetimes of milliseconds when considering only radiative decay. There has long been a desire to better understand and manipulate IVR for coherent control to steer photochemical reactions, to use molecular vibrations in quantum information applications from molecular opto-mechanics, entanglement, and qubits (13, 14) or to realize molecular heat engines harnessing concepts in quantum thermodynamics (6, 15).

Selective mode excitation and spectrally resolving the subsequent energy flow are achieved using IR-pump IR-probe, stimulated Raman, or multidimensional IR spectroscopy. In particular, 2D IR spectroscopy can visualize the transient and coupled vibrational dynamics in molecules (16–23). However, as a third-order nonlinear technique, with generally weak IR vibrational transition moments and unfavorable long wavelength scaling in the IR reducing spatial resolution (24), the associated weak signal limits the approach to large molecular ensembles. Further, mode-selective understanding of IVR within the molecular vibrational manifold has remained a long-standing challenge, and its control via resonant antenna or cavity coupling has emerged as a new frontier (7, 13, 25, 26).

To overcome these limitations, surface-enhanced infrared absorption (SEIRA) and resonant IR antenna–enhanced 2D sum-frequency generation and four-wave mixing have significantly increased analytical sensitivity (27–32). Further, in IR-vibrational

Significance

Ultrafast intramolecular vibrational energy redistribution (IVR) sets fundamental limits to the performance of most functional molecular materials, including photosynthesis, photocatalytic efficiency, polariton chemistry, and quantum coherence in molecular qubits. Conventional approaches to resolving intramolecular vibrational coupling have been limited to large molecular ensembles and lack nanoscale sensitivity and resolution. Here, we pursue a qualitatively different approach through femtosecond infrared vibrational nanospectroscopy of molecules coupled to an infrared active antenna serving as an optical nanocavity. Through the controlled interplay between intrinsic intramolecular coupling and extrinsic Purcell-enhanced modification of vibrational lifetimes, we resolved intramolecular vibrational coupling in nanoscale molecular ensembles. Our work provides a perspective for single-molecule vibrational nanospectroscopy, infrared molecular nanophotonics, and coherent control of vibrational dynamics in quantum chemistry.

scattering scanning near-field optical microscopy (s-SNOM), IR antenna–coupled Purcell-enhanced vibrational relaxation (25, 33, 34) and intermolecular vibrational coupling (35, 36) could be resolved with nanoscale spatial resolution and sensitivity.

Here, we demonstrate how to resolve and control intramolecular vibrational energy redistribution by combining mode-selective vibrational coupling to IR antennas with frequency-selective local probe femtosecond nano-IR spectroscopy. At the example of tunable IR antennas functionalized with a Re–carbonyl complex, with selective excitation of its symmetric and antisymmetric carbonyl vibrations, we resolve intramolecular coupling and its dynamics through the Purcell-enhanced modification of vibrational lifetimes. From a coupled oscillator analysis, modeling the competition between intrinsic intramolecular vibrational coupling and extrinsic antenna-enhanced vibrational relaxation, we derive an IVR rate of (25 ± 8) cm^{-1} corresponding to (450 ± 150) fs. This value is typical for the fast initial energy equilibration between the carbonyl vibrations and is the first step in the cascaded IVR process leading to eventual dephasing and energy dissipation into the many vibrational degrees of freedom of the molecule on the picosecond timescale. In addition, the results suggest that through a combination of frequency-selective antenna and IR excitation, vibrational interference pathways can be controlled to counteract IVR and extend vibrational coherence (anti-Purcell effect). With independent antenna resonance and IR laser frequency degrees of freedom, this approach can be viewed as a linear analogue to 2D IR spectroscopy. With nanoscale spatial resolution and sensitivity down to few hundred molecules, it overcomes both the far-field spatial resolution and sensitivity challenge to measure IVR. In contrast to conventional far-field cavities, including microcavities, which can couple homogeneously to macroscopic ensembles, IR s-SNOM serves as the enabling tool for local-probe spectroscopy of IR antennas as nanocavity resonators with their spatially inhomogeneous antenna–molecule coupling. Our work thus provides a direction for resolving IVR in small molecular ensembles on the nanoscale with a perspective toward single-molecule sensitivity.

Experiment

Conceptually, we measure the free induction decay (FID) of the coupled molecular vibration and nanoantenna mode in IR nanospectroscopy. The vibrational FID component is controlled by the combination of population relaxation (through IVR), pure dephasing, and dephasing due to the inhomogeneously broadened ensemble. As demonstrated previously (33), the population relaxation of a particular vibrational mode ν_i is accelerated through direct Purcell enhancement via modification of the local electromagnetic density of states when the antenna is tuned on resonance with the vibration. In addition, as we show in this work, indirect Purcell enhancement occurs when the antenna is tuned to a different, yet intramolecularly coupled vibration ν_j. If these two modes ν_i and ν_j are not coupled, no such cross-vibrational modification of the vibrational FID rate would be observed. We then derive vibrational coupling and IVR rates from the antenna-frequency dependent enhancement of the FID decay time of one vibrational mode ν_i while selectively coupling the antenna resonance (nanocavity) to another mode ν_j. We develop a coupled oscillator model to fit the FID time based on the spectral evolution of the underlying vibrational population lifetime at the interplay between intrinsic intramolecular coupling (IVR) and extrinsic frequency-tunable antenna-vibration coupling. For our proof-of-concept experiments demonstrating

this nanocavity approach to determine IVR, we choose carbonyl vibrations of the Re–carbonyl complex fac-Re(bpy)(CO)$_3$Cl (bpy = bipyridyl), also known as the Lehn catalyst for photocatalytic CO and CO$_2$ reduction (37–39). The coupled dynamics of the three carbonyl modes of this Re–CO complex have been resolved via multidimensional spectroscopy (40–44) on SiO$_2$ (43) and gold (42). The carbonyl modes exhibit two components contributing to their overall IVR process: An ultrafast energy exchange between the carbonyl modes within hundreds of femtoseconds is followed by their much slower dissipation into the molecular bath on picosecond time scales. Specifically, time-resolved vibrational SFG resolved both the fast ($\sim$260 fs) relaxation between the carbonyl modes and their slow ($\sim$14.8 ps) relaxation into the vibrational manifold of the molecular complex (44). For our experiments, we use gold infrared nanoantennas of variable length tuned to resonance with either the symmetric or antisymmetric carbonyl vibrational stretch modes of the Re–CO complex, which is covalently anchored as a monolayer to the gold metal surface. IR-resonant gold nanoantennas are fabricated as described previously (45) on a CaF$_2$ substrate coated by 100-nm thick Au layer followed by 90 nm MgF$_2$. The resulting ground plane coupling minimizes dissipation resulting in long-lived antennas with narrow linewidth ($\sim$80 cm^{-1} FWHM) corresponding to $T_{\text{FID,ant}}$ $\sim$120 fs lifetimes and Q-factors of $\sim$29 (far-field IR spectra *SI Appendix*). The spatial and spectral field characteristics of the bare and tip-coupled antennas are modeled by finite-difference time-domain (FDTD) simulation. In contrast to conventional far-field cavities, IR antenna nanocavities exhibit spatially inhomogeneous antenna–molecule coupling as determined by antenna dipole mode field distribution and associated near-field electromagnetic local density of states (em-LDOS). This necessitates local probe spectroscopy with nanoscale spatial resolution and associated sensitivity to nanoscale molecular ensembles preferentially probing at the terminal of the antennas where the field enhancement is high.

Infrared scattering-scanning near-field optical microscopy (IR s-SNOM) (Fig. 1A) with interferometric heterodyne detection of the tip scattered near-field is performed as established previously (33). The resulting near-field FID interferograms represent the antenna-coupled vibrational dynamics and are then evaluated in the time domain (46, 47). The corresponding complex-valued Fourier-transformed infrared (nano-FTIR) spectra with near-field amplitude $A_{\text{NF}}(\nu)$ and phase $\Phi_{\text{NF}}(\nu)$ represent the full vibrational response function (47–50).

The molecular monolayer of the rhenium carbonyl complex is prepared by covalent linkage to the nanowire antennas (Fig. 1A) (42) (*SI Appendix*, for details). The complex has two equatorial and one axial CO ligands (Fig. 1B). We perform grazing incidence FTIR measurements (Fig. 1C) as well as nano-FTIR (*SI Appendix*) of the monolayer on a flat gold surface as reference. From Lorentzian fits, we determine the fully symmetric in-phase stretch mode A′(1) at $\bar{\nu}_{\text{A}'(1)} = \bar{\nu}_S = 2{,}028$ cm^{-1} with FWHM$_{\text{A}'(1)} = (16 \pm 3)$ cm^{-1} corresponding to a timescale of $T_{\text{FID,A}'(1)} \simeq 665$ fs. The decay time obtained directly from the nano-FTIR is $T_{\text{FID,A}'(1)} \simeq (750 \pm 100)$ fs, which corresponds to a linewidth of FWHM$_{\text{A}'(1)} = (14 \pm 3)$ cm^{-1}. In the monolayer, the symmetric out-of-phase stretch mode A′(2) at $\bar{\nu}_{\text{A}'(2)} = 1{,}899$ cm^{-1} and the asymmetric stretch of the equatorial ligands A″ at $\bar{\nu}_{\text{A}''} = 2{,}028$ cm^{-1} are spectrally inseparable with A′(2) expected to be the lowest energy mode (41). The spectral widths of both modes are comparable (42), and fitting the spectrum in Fig. 1C results in a FWHM of 32 cm^{-1} each.
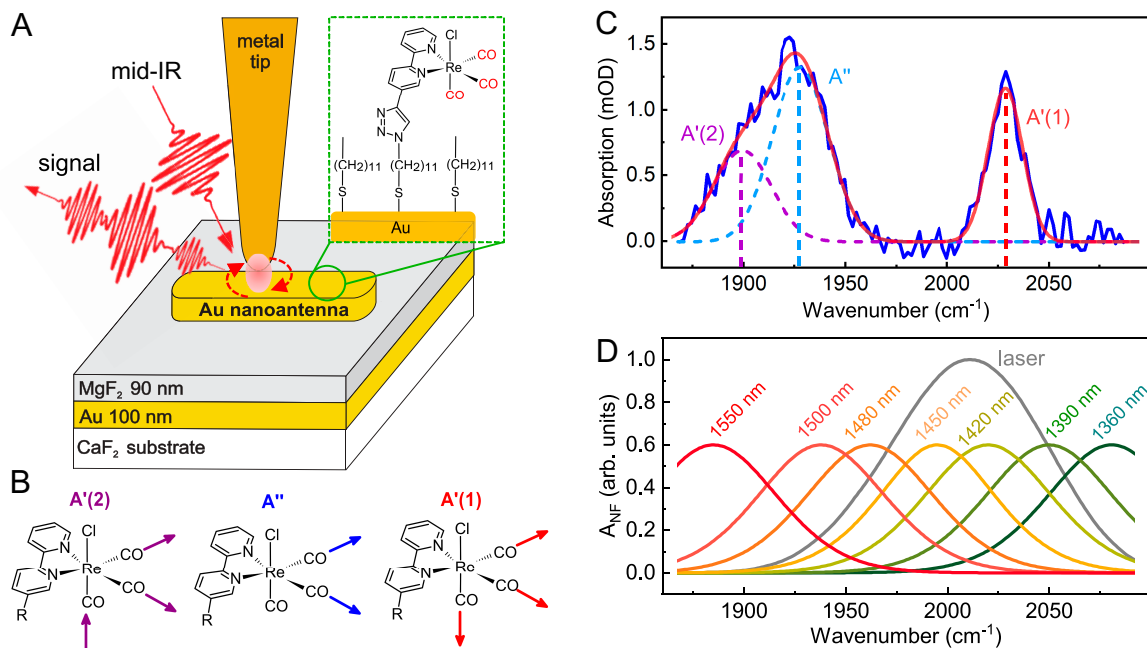
Fig. 1. Purcell-enhanced IR antenna–coupled vibrational spectroscopy. (A) Experimental design of femtosecond IR nanospectroscopy of monolayer Re–carbonyl complex covalently linked to IR gold nanoantenna resonators. (B) Symmetric A′(1), and antisymmetric stretch vibrations A′(2) and A″, of the Re complex (41). (C) Grazing incidence far-field FTIR absorption spectrum with corresponding mode assignment. (D) Near-field amplitude A_{NF} spectra (fitted) of selected infrared nanowire antennas of variable length, with an example laser spectrum.

For the purpose of this study, we thus treat these two lower energy modes as one effective asymmetric mode A′(E) centered at $\bar{\nu}_{A'(E)} = \bar{\nu}_A = 1{,}919$ cm^{-1}. From nano-FID measurement ([*SI Appendix*](#)), we obtain $T_{FID,A'(E)} = (315 \pm 75)$ fs, which corresponds to a linewidth of FWHM$_{A'(E)} = (30 \pm 5)$ cm^{-1}.

The input IR light with a FWHM bandwidth of 100 cm^{-1} and nanoantennas of variable length both tune across the full range of these vibrations (Fig. 1D).

Results

Experiment. We first characterize the antenna near-field distribution by s-SNOM imaging. As an example, Fig. 2A shows AFM topography (*Top*) and two-phase homodyne imaging (*Middle*) at a time delay of $t = 100$ fs for an antenna of length $l = 1{,}400$ nm (corresponding to $\bar{\nu}_{ant} = 2{,}022$ cm^{-1}). The characteristic signal inversion reflects the out-of-phase E_z-field for a dipole

antenna (51). Corresponding FDTD simulation of the absolute field amplitude (*Bottom*) including realistic tip parameters shows only minimal perturbation of the antenna field by the tip due to the resonant antenna response compared to the off-resonant and more weakly polarizable tip response.

We then perform free-induction decay s-SNOM interferometry (*Methods*) of the antenna-coupled molecular response. Fig. 2B (black) shows an interferogram at the example of the laser tuned to the antenna resonance of $\bar{\nu}_{ant} = 2{,}023$ cm^{-1} and the antenna resonant with the A′(1) mode at $\bar{\nu}_{A'(1)} = 2{,}028$ cm^{-1}. Time zero is determined by reference measurement on a planar gold surface as the center of the interferogram for the broadband nonresonant instantaneous response. Due to the resonant nature and finite lifetime of molecular and antenna response, the peak for the resonant interaction is then temporally delayed. The destructive interference and associated beat node near 500 fs is the result of a phase difference between the antenna and vibration(s). With the antenna lifetime shorter than the molecular vibrations, the signal
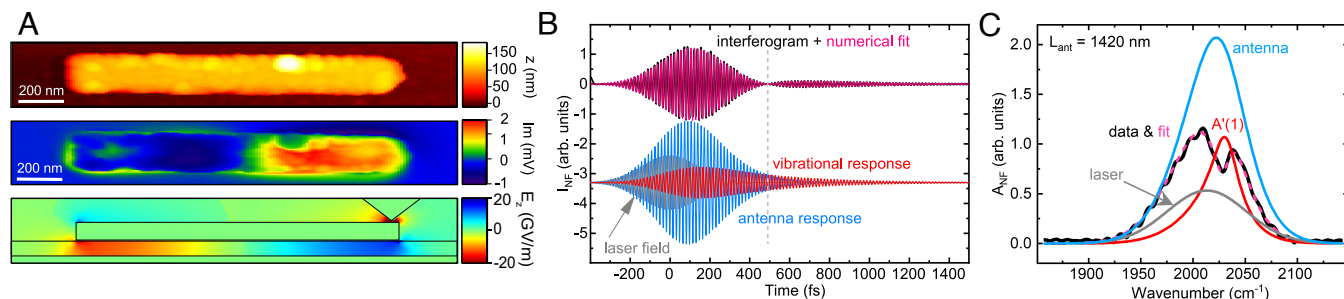

Fig. 2. IR nanoimaging and vibrational free-induction decay of coupled molecular vibrations. (A) AFM topography of nanoantenna (*Top*, l = 1,400 nm), imaginary part of two-phase heterodyne nano-IR imaging (*Middle*), and FDTD calculated E-field amplitude of the antenna–monolayer–tip system (*Bottom*). (B) Corresponding interferogram measured at the right antenna terminal (*Top*, black) with model fit (magenta), and decomposed (*Bottom*) into the driving laser field (gray), the antenna response (blue), and vibrational response (red) of A′(1) mode in this case, and with characteristic distinct lifetime and different relative phases. (C) Corresponding Fourier-transform of time-domain signals in (B). The spectral minimum near the vibrational resonance position is the result of antenna and vibrational interference (Fano resonance).

at long time delays is the isolated vibrational response free from interference artifacts.

In order to extract the individual response functions, we fit the observed interferogram in time-domain as shown in Fig. 2B (*Methods*). The fit (Fig. 2B, magenta), which well describes the experimental data (black), is then decomposed into the individual transients of antenna near-field I_{NF} (blue), molecular vibration (red), and driving laser field (gray). The corresponding Fourier transforms are shown in Fig. 2C. The spectrally narrow feature corresponds to the long-lived molecular vibration, which manifests itself as a spectral dip due to the destructive interference between antenna and molecular vibration as established, Fano interference (33, 52).

We note that despite the principal equivalence of time and frequency domain related by Fourier transform, fitting in the time domain is preferable. This is due to the interference of spectrally closely spaced resonators giving rise to nominally similar superposition spectra, making unambiguous fitting in the frequency domain difficult. In contrast, the decay times of the different contributions to the FID tail are well separated in the time domain.

Systematic IR *s*-SNOM measurements are then performed for a series of antennas with different lengths tuning across both vibrational modes. Fig. 3 shows interferograms for ($l = 1,400$ nm, Fig. 3A), $l = 1,440$ nm (Fig. 3B), and $l = 1,520$ nm (Fig. 3C). Table 1 summarizes the fit results, with uncertainties determined from repeated measurements with slight length variations of the antennas (*SI Appendix* for details).

For the $l = 1,400$-nm antenna with $\bar{\nu}_{ant} = 2,022 \pm 1$ cm^{-1} fully on resonance with A'(1), the antenna-coupled FID of $T_{FID,A'(1)} = 300 \pm 60$ fs is significantly shorter than the intrinsic decay time of $\sim$750 fs of the uncoupled molecules due to the resonant antenna–molecule coupling and associated Purcell enhancement (33). Tuning the antenna to lower frequencies, i.e., away from the A'(1) resonance (Fig. 3B, $\bar{\nu}_{ant} = 1,978$ cm^{-1}), the shape of the interferogram progressively changes. The beating disappears and a signal contribution with fast decay time of $\sim$250 fs from the A'(E) vibration emerges, driven by the onset of an antenna-enhanced excitation via the low-frequency tail of the laser spectrum. Correspondingly, the FID time of the A'(1) vibration rises again due to the progressively weaker coupling between A'(1) and the antenna with the reduced spectral overlap.
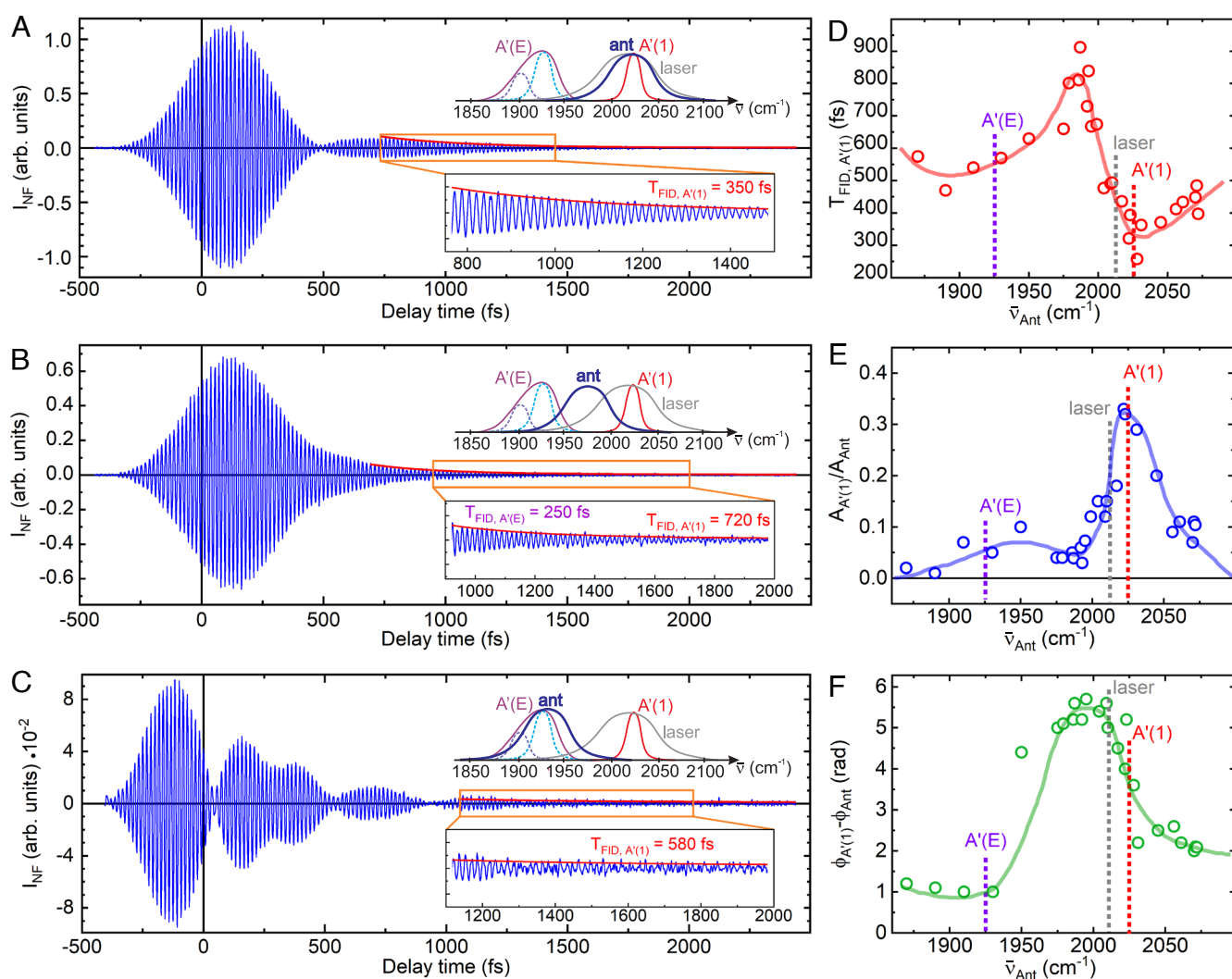

Fig. 3. Antenna-coupled vibrational free-induction decay and IVR. Interferometric nano-IR time traces at a fixed laser excitation frequency of $\bar{\nu}_{Laser} = 2,020$ cm^{-1}, for antennas of variable lengths, with (A) 1,400 nm ($\bar{\nu}_{ant} = 2,022$ cm^{-1}), (B) 1,440 nm antenna ($\bar{\nu}_{ant} = 1,978$ cm^{-1}), and (C) 1,520 nm antenna ($\bar{\nu}_{ant} = 1,937$ cm^{-1}). (D) Extracted T_{FID} decay times of the A'(1) vibrational mode when tuning the antenna frequency. (E) Amplitude of the A'(1) vibrational signal normalized on the antenna signal. (F) Phase difference between the antenna and the A'(1) signal.

Table 1. Nominal antenna length and fit parameters for the interferograms shown in Fig. 3 A–C and Fig. 2B for the antenna frequency $\bar{\nu}_{ant}$, the antenna dephasing time $T_{FID,ant}$, antenna dephasing rate κ_{ant}, the vibrational dephasing time $T_{FID,A'(1)}$, the vibrational dephasing rate γ_S, the amplitude ratio between the vibrational and the antenna signal $A_{A'(1)}/A_{ant}$, and the phase difference between vibration and antenna $\phi_{A'(1)} - \phi_{ant}$

Length (nm)	$\bar{\nu}_{ant}$ (cm^{-1})	$T_{FID,ant}$ (fs)	κ_{ant} (cm^{-1})	$T_{FID,A'(1)}$ (fs)	γ_S (cm^{-1})	$A_{A'(1)}/A_{ant}$	$\phi_{A'(1)} - \phi_{ant}$ (rad)
1,400	$2{,}022 \pm 1$	134 ± 5	79 ± 3	300 ± 60	35 ± 5	0.34 ± 0.11	2.64 ± 0.68
1,440	$1{,}978 \pm 1$	152 ± 5	70 ± 3	680 ± 130	16 ± 4	0.046 ± 0.014	0.74 ± 0.55
1,520	$1{,}937 \pm 5$	120 ± 5	88 ± 3	500 ± 100	21 ± 4	0.019 ± 0.008	0.54 ± 0.61

The vibrational frequency is fixed to $\bar{\nu}_{A'(1)} = 2{,}028$ cm^{-1}. The parameters for the laser field are identical for this dataset with a laser frequency of $\bar{\nu}_{Laser} = 2{,}013$ cm^{-1} and a FWHM pulse duration of $t = 167$ fs, which we assume to possess no significant chirp. Individual values are the average of fit parameters from 5 consecutive scans. The variance is calculated from at least 4 independent measurements.

Shifting the antenna frequency toward resonance with A'(E) to $\bar{\nu}_{ant} = 1{,}937$ cm^{-1} (Fig. 3C), now with antenna resonant with A'(E) and the laser with A'(1), both vibrational modes contribute, which gives rise to a complex interference behavior. Significantly, the FID time of the A'(1) vibration is again reduced to $T_{FID,A'(1)} = 500 \pm 100$ fs. This recurring decrease of $T_{FID,A'(1)}$ indicates the acceleration of the vibrational decay through the antenna-mediated relaxation acceleration of A'(E). This behavior is the signature of the intramolecular vibrational coupling between A'(E) and A'(1) and associated IVR process between these.

The results for the systematic variation of antenna frequencies and derived parameters for the A'(1) vibration are summarized in Fig. 3 D–F for the fixed laser excitation centered at 2,013 cm^{-1}. The cross-vibrational decrease in vibrational FID time is accompanied by a global A'(1) and local A'(E) signal maximum (Fig. 3E). Further, a π phase shift is observed when tuning the antenna across the vibrational resonance as expected (Fig. 3F).

Theory and Modeling

The FID is controlled by population relaxation T_1, pure dephasing T_2^*, and inhomogeneous broadening. The inhomogeneous broadening, typically given by a statistical Gaussian distribution, can be approximated as Lorentzian disorder as shown previously (53). The FID decay time can then be written as $1/T_{FID} = 1/2T_1^0 + 1/T_2^* + 1/T_{inhom}$, giving rise to a single exponential response of the vibrational signal in time domain as $I_{NF}(t) \propto \exp(-t/T_{FID})$. We can assume T_2^* and T_{inhom}, in the absence of a fast-fluctuating solvent environment, to arise largely from intermolecular interactions. From previous work (42, 43), T_2^* can be estimated to range from ∼4 to ∼8 ps (*SI Appendix*). T_2^* thus contributes only weakly to the total decay time and does not have a measurable effect on the fast FID decay. Further, it is largely unaffected by the antenna coupling and is spatially homogeneous within the monolayer across and between antennas. T_2^* is thus assumed to be constant for the purpose of our study, with little variations between antennas in monolayer density and structure as seen from IR s-SNOM imaging.

As expected, inhomogeneous broadening T_{inhom} ranging from 500 fs to 750 fs (42, 43) dominates the vibrational FID decay. We see little variations between antennas in IR s-SNOM imaging, suggesting a homogeneous monolayer density. T_{inhom} is dominated by local structural heterogeneities leading to the underlying statistical distribution in vibrational frequencies. T_{inhom} and T_2^* are therefore not expected to change when length-tuning the antenna frequency.

Therefore, we assume only T_1 of the vibrational modes is modified when tuning the resonance of the antenna across that same vibrational mode or a coupled vibrational mode from which we derive IVR. For the interpretation and the derivation of the IVR rate from the antenna-enhanced $1/T_{FID}$ of coupled molecular vibrations, it is important to note that the antenna spectrum is broad compared to the vibrational linewidth and therefore all molecular subensembles within the linewidth are equally affected by the antenna.

In order to quantify the intramolecular coupling rate from the measured antenna-enhanced cross-vibrational modification of $T_{FID,A'(1)}$, we apply a coupled oscillator model for the antenna and the symmetric A'(1) and asymmetric A'(E) vibrations, with their respective vibration–antenna coupling g_S and g_A, a bilinear intramolecular vibration–vibration interaction rate ζ_{SA} (IVR), and antenna and vibrational relaxation rates κ_{ant}, γ_S, and γ_A, respectively. We assume that the laser field primarily drives the antenna mode which in turn excites the molecular vibrations (25, 34). We then fit the antenna frequency dependence of $T_{FID,A'(1)}$ with the IVR rate ζ_{SA} as the only free parameter. All other parameters are constrained, including molecular-antenna coupling determined from the Purcell enhancement of the vibrational resonance and antenna and vibrational frequencies, and decay rates predetermined from the reference measurements of a bare antenna and molecular monolayer on the planar gold surface.

The coupled rate equations follow from $\dot{\mathbf{Y}}(t) = -\mathbf{M}\mathbf{Y}(t) + \mathbf{F}(t)$, with the mean-field vector $\mathbf{Y} = [\langle \hat{B}_S \rangle, \langle \hat{a} \rangle, \langle \hat{B}_A \rangle]^T$, describing the joint evolution of the symmetric mode A'(1) given by $\langle \hat{B}_S \rangle$, the antenna field $\langle \hat{a} \rangle$, and the asymmetric mode A'(E) given by $\langle \hat{B}_A \rangle$. $\mathbf{M}$ is given by

$$\mathbf{M} = \begin{pmatrix} \gamma_S/2 + i\omega_S & ig_S & i\zeta_{SA} \\ ig_S & \kappa_{ant}/2 + i\omega_{ant} & ig_A \\ i\zeta_{SA} & ig_A & \gamma_A/2 + i\omega_A \end{pmatrix}, \quad [1]$$

with A'(1) frequency $\omega_S = 2\pi c \bar{\nu}_{A'(1)}$ with $\bar{\nu}_{A'(1)} = 2{,}028$ cm^{-1}, and g_S the coupling rate constant with the antenna. The corresponding parameters for A'(E) are $\omega_A = 2\pi c \bar{\nu}_{A'(E)}$ with $\bar{\nu}_{A'(E)} = 1{,}919$ cm^{-1}, and g_A. The uncoupled antenna frequency and its decay rate are $\omega_{ant} = 2\pi c \bar{\nu}_{ant}$ and κ_{ant}, respectively (34).

From the dynamical matrix $\mathbf{M}$, we then derive analytical expressions for leading contributions to $T_{FID,A'(1)}$ and $T_{FID,A'(E)}$. For both vibrational modes, the total decay time can be approximated as

$$1/T_{FID} \approx 1/T_{FID}^0 + 1/2T_{1,P} + 1/2T_{1,IVR-P} + 1/2T_{1,anti-P}, \quad [2]$$

where each term has specific dependence on the model parameters. In the following, we describe the individual contributions to the vibrational decay time $T_{FID,A'(1)}$. For equivalent expressions for the A'(E) mode see *SI Appendix*.

The first term in Eq. **2** corresponds to vibrational relaxation in the absence of antenna coupling, which for the A'(1) mode is given by $1/T_{FID}^0 = \gamma_S/2 + 2\zeta_{SA}^2 \Delta\gamma/[(\Delta\gamma)^2 + 4\Delta_{SA}^2]$, with $\Delta\gamma \equiv \gamma_S - \gamma_A$, and $\Delta_{SA} = \omega_A - \omega_S$.

The second term describes the antenna-induced Purcell enhancement of the vibrational relaxation. For A'(1), this reads $1/2T_{1,P} = 2g_S^2\Delta\Gamma/[(\Delta\Gamma)^2 + 4\Delta_{antS}^2]$, with $\Delta\Gamma \equiv \kappa_{ant} - \gamma_S$, and detuning $\Delta_{antS} = \omega_{ant} - \omega_S$ (34). This contribution is largest (i.e., lowest values of T_1) for resonant antenna–molecule coupling ($\Delta_{antS} = 0$) and is responsible for the primary $T_{FID,A'(1)}$ minimum in Fig. 4A at the A'(1) frequency.

The third term in Eq. **2** describes the cross-vibrational coupling that gives rise to the off-diagonal decrease in relaxation

Fig. 4. (A) Vibrational dephasing time $T_{FID,A'(1)}$ of the symmetric A'(1) mode subject to laser driving at 2,020 cm^{-1}, as a function of antenna resonance frequency ω_{ant}. Experiment (circles) and analytical results with (solid blue line) and without (solid gray line) anti-Purcell effect. For fixed antenna and molecular parameter of $\gamma_S = 14$ cm^{-1}, $\bar{\nu}_{A'(1)} = 2,028$ cm^{-1}, $\gamma_A = 30$ cm^{-1}, $\bar{\nu}_{A'(E)} = 1,919$ cm^{-1}, $\kappa_{ant} = 80$ cm^{-1}, $g_S = 20$ cm^{-1}, $g_A = 2.7g_S$, and $\eta = 0.5$, a vibration–vibration coupling rate $\zeta_{SA} = 25 \pm 8$ cm^{-1} is derived. (B) Evolution of T_{FID} time of the effective A'(E) vibrational mode for laser driving at 1,919 cm^{-1}.

time and is responsible for the second minimum at the A'(E) frequency shown in Fig. 4A. It corresponds to an effective cavity-induced acceleration of vibrational relaxation through the bilinear intervibrational coupling. This contribution can be written as

$$\frac{1}{2T_{1,IVR-P}} = \frac{4\zeta_{SA}^2 g_S^2 \kappa_{ant}}{[(\Delta\gamma)^2 + 4\Delta_{SA}^2][\kappa_{ant}^2 + 4\Delta_{antA}^2]}, \quad [3]$$

where $\Delta_{antA} \equiv \omega_{ant} - \omega_A$ is the antenna detuning from the asymmetric A'(E) mode. This term is largest when $\Delta_{antA} = 0$, which gives rise to a local minimum in $T_{FID,A'(1)}$ at the A'(E) frequency.

The last contribution to Eq. **2** is a higher-order process obtained by artificially turning off the intrinsic vibration–vibration coupling ($\zeta_{SA} \to 0$). In this case, the coupling of the A'(1) and A'(E) modes to the common antenna field induces an effective vacuum-mediated interaction between the two modes, which in turn contributes to the modification of the coupled relaxation pathways for each vibration. If the Rabi coupling of the A'(E) mode is large enough, this effective field-mediated interaction can interfere and compete with the Purcell effect of the A'(1) mode and effectively increase the vibrational dephasing time. This anti-Purcell contribution can be written as

$$\frac{1}{2T_{1,anti-P}}$$
$$= \eta \, Re \left\{ \frac{g_S^2[\Delta\gamma/2 + i\Delta_{SA}]}{g_A^2 + g_S^2 - [\Delta\gamma/2 + i\Delta_{SA}][\Delta\Gamma/2 + i\Delta_{antS}]} \right\}, \quad [4]$$

where we introduce an empirical weighting factor ($0 < \eta < 1$) to control the degree by which this term is relevant in a system where both intrinsic and field-mediated vibration–vibration couplings coexist. For a system with $\zeta_{SA} = 0$, for consistency with the assumptions above, we must set $\eta = 1$.

For the model fit to the data shown in Fig.4A, we use $\gamma_S = FWHM_{A'(1)} = 14$ cm^{-1}, $\bar{\nu}_{A'(1)} = 2,028$ cm^{-1}, $\gamma_A = FWHM_{A'(2)/A''} = 30$ cm^{-1}, $\bar{\nu}_{A'(E)} = 1,919$ cm^{-1}, and $\kappa_{ant} = 80$ cm^{-1} fixed as discussed above (Table 1). We obtain vibration–antenna couplings $g_S = 20$ cm^{-1} and $g_A = 2.7g_S$ from the respective on resonance Purcell-enhanced reduction in lifetime, which are independent of the vibration–vibration coupling. We obtain the anti-Purcell factor of $\eta = 0.5$ from the increased lifetime for antenna resonances in between vibrational modes (Fig. 5C). With these parameters constrained, the remaining frequency-dependent reduction in A'(1) lifetime is only controlled by the vibration–vibration coupling that we obtain by least-square optimization on the data to $\zeta_{SA} = (25 \pm 8)$ cm^{-1}. The fit is shown in Fig. 4A with (blue line) and without (gray line) the anti-Purcell effect. The analytical model well reproduces the experimental results, and the IVR rate constant derived is in good agreement with literature values for the carbonyl vibrations of the Re–carbonyl complex as discussed below. In Fig. 4B, we model the experimental data for the decay of A'(E) with $\eta = 0$ but otherwise the same fit parameters as in Fig. 4A. The frequency offset of the model (blue) with respect to the experimental data might be due to our treatment of the two vibrational modes (A'' and A'(2)) as the effective mode A'(E), yet the expected Purcell enhanced relaxation is observed qualitatively. We attribute the difficulty in observing the second dip at A'(1) to the shorter intrinsic lifetime of the A'(E) mode (*SI Appendix*, *Theory*).

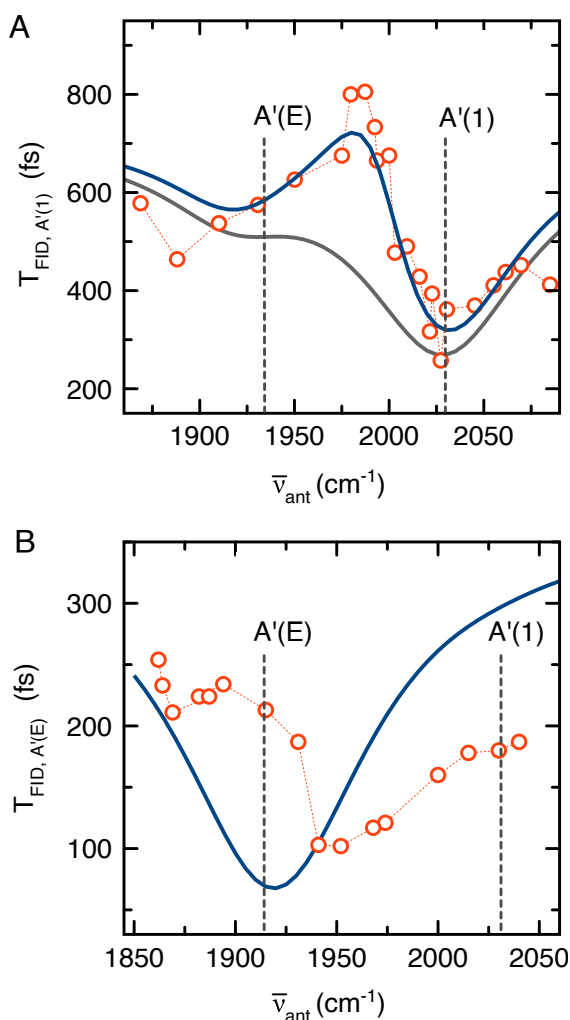Note that, up to a global phase, Eq. **4** is formally equivalent to the absorptive response of an atomic probe transition under

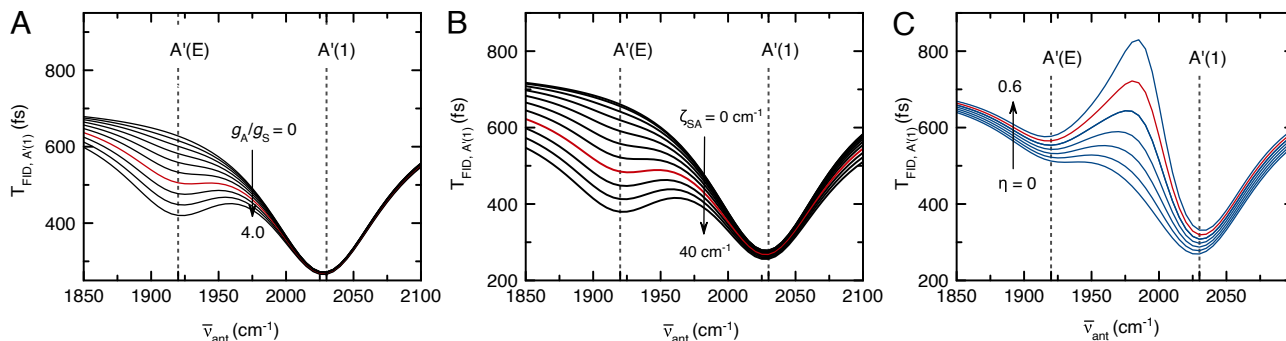**Fig. 5.** Model $T_{FID,A'(1)}$ as a function of antenna frequency $\bar{\nu}_{Ant}$, obtained from $1/T_{FID}^0 + 1/2T_{1,P} + 1/2T_{1,IVR-P}$. (*A*) For varying ratios of the oscillator strengths $0 \leq g_A/g_S \leq 4.0$, for fixed vibration–vibration coupling $\zeta_{SA} = 25$ cm^{-1}, $g_S = 20$ cm^{-1} and weighting anti-Purcell factor $\eta = 0$. (*B*) For varying $0 \leq \zeta_{SA} < 40$ cm^{-1}, with fixed ratio $g_A/g_S = 3.3$ and $\eta = 0$. (*C*) For varying $0 \leq \eta < 0.6$, $g_A/g_S = 2.7$ and $\zeta_{SA} = 25$ cm^{-1}. The red marked lines correspond to the parameters with the best fit to the experimental data in Fig. 4*A*.

electromagnetically induced transparency (EIT) (54), with A′(E) to antenna coupling g_A acting as the control field for the A′(1) light–matter interaction. This predicts an increase of $T_{FID,A'(1)}$ above the far-field (field-free) limit for A′(1) over a narrow antenna frequency window. Indeed, the better agreement of the anti-Purcell model with the data for antenna frequencies in the region near 1,980 cm^{-1} with $T_{FID} > 750$ fs would support the presence of this mechanism.

In Fig. 5, we analyze the individual processes that contribute to $T_{FID,A'(1)}$ according to Eq. **2**. The sum of $1/T_{FID}^0 + 1/2T_{1,P} + 1/2T_{1,IVR-P}$ provides for a good qualitative description for the emergence of the second minimum in $T_{FID,A'(1)}$ at $\bar{\nu}_{ant} = \bar{\nu}_{A'(E)}$. Eq. **3** predicts the decrease in $T_{FID,A'(1)}$ at the A′(E) frequency to scale as $(\zeta_{SA}/\Delta_{SA})^2(g_A/g_S)^2$, suggesting that ζ_{SA} can be quantified from the second T_2 minimum if the oscillator strengths of the driven and undriven vibrations are known. On the other hand, since the antenna field is the same for both modes, the relative depth of the two T_{FID} minima is determined by the ratio of the two oscillator strengths, i.e., $(g_A/g_S)^2 \approx d_A^2/d_S^2$, where d_A and d_S are transition dipoles. To illustrate this behavior, Fig. 5*A* shows that by increasing the coupling strength g_A of the asymmetric mode ($\propto d_A$), while leaving all other parameters fixed, the off-resonant $T_{FID,A'(1)}$ minimum becomes progressively more pronounced. Conversely, if both the ratio $g_A/g_S \approx 2.7$ and $\Delta_{SA} \approx 100$ cm^{-1} are fixed and ζ_{SA} is varied, Fig. 5*B* shows how the variation of the second minimum then serves as a way to resolve IVR through the effect of selective vibrational antenna coupling. In Fig. 5*C*, the weighting factor η is varied to illustrate the contribution of the anti-Purcell effect.

Discussion

The experiments demonstrate modification of vibrational lifetimes of the antenna-coupled symmetric and antisymmetric Re–carbonyl CO vibrations by selective and independent tuning of antenna resonance and driving laser frequency to resolve intramolecular coupling and its dynamics through the Purcell-enhanced modification of vibrational lifetimes in competition with IVR and antenna coupling. The derived intramolecular coupling constant $\zeta_{SA} = (25 \pm 8)$ cm^{-1} corresponds to a time scale for the energy exchange between the CO modes of $T_{IVR} = 1/c\pi\zeta_{SA} = 450 \pm 150$ fs. Various molecular systems with carbonyl modes are known for stronger coupling (21, 55), and timescales of a few hundred femtoseconds are consistent with

theoretical IVR models (56). Specifically for the Re-complex, time-resolved measurements of the IVR time can be found in time-resolved SFG measurement from Anfuso et al. (44), where the equilibration time is measured to 260 fs. They estimate an uncertainty of 100 fs for their IVR time constant, which may in fact be optimistic, considering the sparse number of data points around time zero and a time resolution (IRF) of 180 fs. But even considering their value of (260 ± 100) fs, our results would be in agreement with the uncertainties of both experiments. Some differences would also be expected considering the different anchoring of the monolayer.

Traditionally, resolving IVR requires 2D IR or nonlinear Raman techniques with coupling pathways manifesting themselves as cross-peaks in multidimensional frequency space (21, 57, 58). IR active optical antennas have been utilized in 2D IR, yet only for the purpose of signal enhancement or in strong coupling (29, 30, 32, 57, 59, 60). What distinguishes our approach is the independent tuning of antenna and laser frequency, enabling the separation of mode-selective coupling and driving the excitation. While 2D IR spectroscopy directly monitors the vibrational population transfer in IVR, here, we infer it indirectly through the tunable antenna-induced mode-selective modification of the free-induction decay caused by underlying changes in the lifetime of coupled vibrations. This provides a conceptual analogue to coherent third-order 2D IR spectroscopy, where we replace one of the two laser frequency axes with the antenna frequency. This lifts the degeneracy of conventional first-order IR spectroscopy and provides access to the mode coupling.

However, the linear response approach is unable to drive and monitor vibrational ladder-climbing processes and is lacking direct access to vibrational population. Future extensions of the scheme involving two or more intense femtosecond pulses would allow for exploration of vibrational excited state dynamics and population transfer between light and matter states. These insights are essential to understand emergent coherent phenomena such as polariton condensation and photon lasing, which have been well studied with exciton–polaritons (61) but remain to be seen in the infrared.

Our experimental approach is not restricted to weak coupling using IR antennas as resonators. It should work equally well in cavity resonators both in weak and strong coupling by selectively tuning the cavity resonance across vibrational modes of interest and cross-driving the modes not coupled to the cavity. This could prove advantageous for exploring the degree by which global observables such as an IR cavity spectrum of the coupled

vibration-cavity system can correlate with the local intramolecular and intermolecular coherence transfer processes that influence the rate of chemical reactions. This question has been the subject of many experimental studies in recent years (62), primarily using diffraction-limited Fabry–Perot infrared cavities (60, 63–65). Here, linear nano-IR spectroscopy, combined with quantum modeling, can provide values of the Rabi couplings, vibrational dephasing times, cavity photon lifetimes, and vibrational energy transfer rates that together offer a description of the intracavity light–matter dynamics that is comparable with the information obtained using multidimensional IR spectroscopy in Fabry–Perot cavities (65).

The linear response analysis already captures classical phase effects that emerge when the response of different oscillators coherently interferes in time the domain resulting in Fano line-shapes in the Fourier domain (66). These phase effects are fully accounted for in our analysis and are independent of the Purcell-enhanced modification of the dephasing time of the vibrational resonances (34, 67), as we separate the vibrational phase evolution from the exponential envelope evolution as shown in Fig. 3. The formalism can readily be extended to include higher-order classical dynamics such as population (energy) transfer as well as nonclassical effects such as infrared squeezing (34).

The advantage of open nanoantennas and nanoprobe detection over far-field transmission measurements with Fabry–Perot cavities for strong coupling is the ability to reach simultaneous femtosecond and nanometer spatiotemporal resolution (68, 69). The nanocavity approach for strong coupling allows, for example, unraveling the complex space-dependent energy transfer pathways that emerge in strong coupling between delocalized polaritonic states and semilocalized material states (70, 71), using much smaller molecular ensembles than those available in Fabry–Perot cavities. With significant signal intensities probing already as low as few 100 molecules estimated from the carbonyl density in the monolayer, and given the N scaling of the FID trace amplitude, we readily expect to reach the subergodic regime at $N \sim 10 - 100$. With further improved antenna designs employing larger field confinement and lower photon losses, we believe the few-molecule limit to be within reach.

In summary, our work provides a nanospectroscopic approach to resolve intramolecular coupling and energy transfer through vibrational mode-selective infrared antenna coupling in small molecular ensembles on the nanoscale. As a nanoimaging technique, it would be informative in the application to photosynthesis, photocatalysis, polariton chemistry, and the study of vibrational quantum coherence. With the perspective toward single-molecule sensitivity and single-vibration strong coupling, antenna-coupled cross-vibrational nanospectroscopy would stimulate paradigm shifts in single-molecule detection, mode resolved vibrational coupling, vibrational quantum dynamics, and its control.

Materials and Methods

IR S-SNOM. The homebuilt nano-FTIR IR s-SNOM setup as described previously (35, 36, 72) consists of an atomic force microscope (AFM) combined with an asymmetric Michaelson interferometer (nanoIR2-s prototype, Bruker/Anasys Instruments), with dry-air purge enclosure. Tunable mid-IR $\sim$150 fs femtosecond laser pulses are provided by frequency conversion of a Yb:KGW fiber oscillator pulse laser (1,030 nm center wavelength, 76 MHz repetition rate, 6.5 W output power, FLINT from Light Conversion), pumping an optical parametric oscillator (Levante OPO, APE), with subsequent difference frequency generation (DFG) (HarmoniXX DFG, APE) of the near-infrared signal and idler beams. The IR light after passing a BaF$_2$ beamsplitter is focused onto a platinum/iridium tip (ARROW NCPt, NanoWorld) with an off-axis parabolic mirror with an angle

of incidence of $\sim$ 60° regarding the tip axis. The incidence IR light is polarized parallel with respect to the tip axis (p-polarized with respect to the optical plane). The polarization is projected along the long axis of the antenna. The tip-scattered field of near-field origin is heterodyne-amplified by a reference pulse and detected by an MCT detector (KLD-0.5-J1/DC/11, Kolmar Technologies). It is demodulated at the 2nd harmonic of the AFM cantilever tapping frequency (HF2LI Lock-In, Zurich Instruments) providing asymmetric vibrational free-induction decay interferograms measured by controlling the time delay of the reference field with a precision translation stage (ANT95-50-L-MP, Aerotech). A BaF$_2$ substrate in the reference arm is used to compensate for the dispersion of the beam splitter.

Response Function Fit. We consider that the measured heterodyne intensity signal is the cross-correlation between the near-field E_{NF} and the reference field E_{ref} (33) with time delay τ and given by

$$I_{FID}(\tau) \propto \int_{-\infty}^{\infty} E_{NF}(t) E_{ref}^*(t-\tau) dt. \quad [5]$$

We model the near-field E_{NF} as the superposition of the antenna response and the two vibrational modes A′(1) and A′(E) folded with the driving laser field:

$$
\begin{aligned}
E_{NF}(t) \propto \ & \bar{A}_{ant} e^{-i\bar{\phi}_{ant}} \int_{-\infty}^{\infty} \bar{g}_{ant}(t-t') E_{in}(t') dt' \\
& + \bar{A}_{A'(1)} e^{-i\bar{\phi}_{A'(1)}} \int_{-\infty}^{\infty} \bar{g}_{A'(1)}(t-t') E_{in}(t') dt' \quad [6] \\
& + \bar{A}_{A'(E)} e^{-i\bar{\phi}_{A'(E)}} \int_{-\infty}^{\infty} \bar{g}_{A'(E)}(t-t') E_{in}(t') dt'.
\end{aligned}
$$

Here, $\bar{A}_j$ is the amplitude, $\bar{\phi}_j$ the phase, and $\bar{g}_j(t)$ the response functions, respectively. The driving field $E_{in}(t)$ of the infrared pulse is equivalent to the reference field (*SI Appendix*). The bar denotes a parameter change from the intrinsic value dependent on the antenna-vibration coupling strength. The response function at the example of the A′(1) vibration is given by

$$\bar{g}_{A'(1)}(t) = \frac{1}{2\bar{\omega}_{A'(1)}} \exp\left(-\frac{t}{\bar{T}_{FID,A'(1)}}\right) \exp\left(-i\bar{\omega}_{A'(1)} t\right) \theta(t), \quad [7]$$

assuming a harmonic oscillator with center frequency $\bar{\omega}_j$ and coherence time $T_{FID,j}$. $\theta(t)$ is a Heaviside step function to account for exponential decay of the excited states only after the excitation.

Data, Materials, and Software Availability. The procedures of experiments and simulations are described in the *Materials and Methods* section and in the *SI Appendix*. Data, computer code for fitting, and modeling code are available through the Open Science Frame repository (https://osf.io/rhnmz/) (73).

Author affiliations: ^{a}Department of Physics, and JILA, University of Colorado, Boulder, CO 80309; ^{b}Department of Physics, Universidad de Santiago de Chile, Estación Central 917022, Chile; ^{c}Institute of Bioengineering, École Polytechnique Fédéral de Lausanne, Lausanne 1015, Switzerland; ^{d}Department of Chemistry, University of Colorado, Boulder, CO 80309; and ^{e}Millennium Institute for Research in Optics, Concepción 4030000, Chile

1. P. R. Stannard, W. M. Gelbart, Intramolecular vibrational energy redistribution. *J. Phys. Chem.* **85**, 3592–3599 (1981).
2. T. Uzer, W. H. Miller, Theories of intramolecular vibrational energy transfer. *Phys. Rep.* **199**, 73–146 (1991).
3. D. J. Nesbitt, R. W. Field, Vibrational energy flow in highly excited molecules: Role of intramolecular vibrational redistribution. *J. Phys. Chem.* **100**, 12735–12756 (1996).
4. R. Bigwood, M. Gruebele, D. M. Leitner, P. G. Wolynes, The vibrational energy flow transition in organic molecules: Theory meets experiment. *Proc. Natl. Acad. Sci. U.S.A.* **95**, 5960–5964 (1998).
5. M. Gruebele, R. Bigwood, Molecular vibrational energy flow: Beyond the Golden Rule. *Int. Rev. Phys. Chem.* **17**, 91–145 (1998).
6. D. M. Leitner, Quantum ergodicity and energy flow in molecules. *Adva. Phys.* **64**, 445–517 (2015).
7. K. D. Park *et al.*, Variable-temperature tip-enhanced Raman spectroscopy of single-molecule fluctuations and dynamics. *Nano Lett.* **16**, 479–487 (2016).
8. S. Karmakar, S. Keshavamurthy, Intramolecular vibrational energy redistribution and the quantum ergodicity transition: A phase space perspective. *Phys. Chem. Chem. Phys.* **22**, 11139–11173 (2020).
9. R. A. Marcus, Unimolecular dissociations and free radical recombination reactions. *J. Chem. Phys.* **20**, 359–365 (1951).
10. R. A. Marcus, O. K. Rice, Session on free radicals the kinetics of the recombination of methyl radicals and iodine atoms. *J. Phys. Coll. Chem.* **55**, 894–908 (1951).
11. H. M. Rosenstock, M. B. Wallenstein, A. L. Wahrhaftig, H. Eyring, Absolute rate theory for isolated systems and the mass spectra of polyatomic molecules. *Proc. Natl. Acad. Sci. U.S.A.* **38**, 667–678 (1952).
12. N. B. Slater, New formulation of gaseous unimolecular dissociation rates. *J. Chem. Phys.* **24**, 1256–1257 (1956).
13. C. M. Tesch, R. de Vivie-Riedle, Quantum computation with vibrationally excited molecules. *Phys. Rev. Lett.* **89**, 157901 (2002).
14. S. T. Velez *et al.*, Preparation and decay of a single quantum of vibration at ambient conditions. *Phys. Rev. X* **9**, 041007 (2019).
15. L. Cui *et al.*, Thermal conductance of single-molecule junctions. *Nature* **572**, 628–633 (2019).
16. P. Hamm, M. Lim, R. M. Hochstrasser, Structure of the amide I band of peptides measured by femtosecond nonlinear-infrared spectroscopy. *J. Phys. Chem. B* **102**, 6123–6138 (1998).
17. S. Mukamel, Multidimensional femtosecond correlation spectroscopies of electronic and vibrational excitations. *Annu. Rev. Phys. Chem.* **51**, 691–729 (2000).
18. J. Bredenbeck, J. Helbing, C. Kolano, P. Hamm, Ultrafast 2D-IR spectroscopy of transient species. *Chem. Phys. Chem.* **8**, 1747–1756 (2007).
19. D. V. Kurochkin, S. R. G. Naraharisetty IV, Rubtsov,, A relaxation-assisted 2D IR spectroscopy method. *Proc. Natl. Acad. Sci. U.S.A.* **104**, 14209–14214 (2007).
20. P. Hamm, M. T. Zanni, *Concepts and Methods of 2D Infrared Spectroscopy* (Cambridge University Press, 2011).
21. C. R. Baiz *et al.*, Vibrational spectroscopic map, vibrational spectroscopy, and intermolecular interaction. *Chem. Rev.* **120**, 7152–7218 (2020).
22. N. M. Kearns, R. D. Mehlenbacher, A. C. Jones, M. T. Zanni, Broadband 2D electronic spectrometer using white light and pulse shaping: Noise and signal evaluation at 1 and 100 kHz. *Opt. Exp.* **25**, 7869 (2017).
23. A. Tokmakov, *Nonlinear and Two-Dimensonal Spectrsocopy* (LibreTexts, 2022).
24. C. R. Baiz, D. Schach, A. Tokmakoff, Ultrafast 2D IR microscopy. *Opt. Exp.* **22**, 18724 (2014).
25. E. A. Muller *et al.*, Nanoimaging and control of molecular vibrations through electromagnetically induced scattering reaching the strong coupling regime. *ACS Photon.* **5**, 3594–3600 (2018).
26. M. D. Tt. Chen, Z. Yang, J. Yuen-Zhou, W. Xiong, Cavity-enabled enhancement of ultrafast intramolecular vibrational redistribution over pseudorotation. *Science* **378**, 790–794 (2022).
27. D. Rodrigo *et al.*, Mid-infrared plasmonic biosensing with graphene. *Science* **349**, 165–168 (2015).
28. O. Selig, R. Siffels, Y. L. Rezus, Ultrasensitive ultrafast vibrational spectroscopy employing the near field of gold nanoantennas. *Phys. Rev. Lett.* **114**, 1–5 (2015).
29. F. Neubrech, C. Huck, K. Weber, A. Pucci, H. Giessen, Surface-enhanced infrared spectroscopy using resonant nanoantennas. *Chem. Rev.* **117**, 5110–5145 (2017).
30. R. T. Mackin *et al.*, Surface-enhanced dual-frequency two-dimensional vibrational spectroscopy of thin layers at an interface. *J. Phys. Chem. C* **122**, 11015–11023 (2018).
31. A. Gandman, R. T. Mackin, B. Cohn IV, L Chuntonov Rubtsov, Radiative enhancement of linear and third-order vibrational excitations by an array of infrared plasmonic antennas. *ACS Nano* **12**, 4521–4528 (2018).
32. L. Chuntonov IV, Rubtsov,, Surface-enhanced ultrafast two-dimensional vibrational spectroscopy with engineered plasmonic nano-antennas. *J. Chem. Phys.* **153**, 050902 (2020).
33. B. Metzger *et al.*, Purcell-enhanced spontaneous emission of molecular vibrations. *Phys. Rev. Lett.* **123**, 153001 (2019).
34. J. F. Triana *et al.*, Semi-empirical quantum optics for mid-infrared molecular nanophotonics. *J. Chem. Phys.* **156**, 124110 (2022).
35. E. A. Muller *et al.*, Vibrational exciton nanoimaging of phases and domains in porphyrin nanocrystals. *Proc. Natl. Acad. Sci. U.S.A.* **117**, 7030–7037 (2020).
36. T. P. Gray, J. Nishida, S. C. Johnson, M. B. Raschke, 2D vibrational exciton nanoimaging of domain formation in self-assembled monolayers. *Nano Lett.* **21**, 5754–5759 (2021).
37. J. Hawecker, J. M. Lehn, R. Ziessel, Electrocatalytic reduction of carbon dioxide mediated by Re(bipy)(CO)3 Cl (bipy = 2,2′-bipyridine). *J. Chem. Soc. Chem. Commun.* **3**, 328–330 (1984).
38. A. J. Morris, G. J. Meyer, E. Fujita, Molecular approaches to the photocatalytic reduction of carbon dioxide for solar fuels. *Acc. Chem. Res.* **42**, 1983–1994 (2009).
39. M. D. Sampson *et al.*, Direct observation of the reduction of carbon dioxide by rhenium bipyridine catalysts. *Energy Environ. Sci.* **6**, 3748–3755 (2013).
40. M. Delor *et al.*, Dynamics of ground and excited state vibrational relaxation and energy transfer in transition metal carbonyls. *J. Phys. Chem. B* **118**, 11781–11791 (2014).
41. L. M. Kiefer, J. T. King, K. J. Kubarych, Dynamics of rhenium photocatalysts revealed through ultrafast multidimensional spectroscopy. *Acc. Chem. Res.* **48**, 1123–1130 (2015).
42. C. Yan *et al.*, Unraveling the dynamics and structure of functionalized self-assembled monolayers on gold using 2D IR spectroscopy and MD simulations. *Proc. Natl. Acad. Sci. U.S.A.* **113**, 4929–4934 (2016).
43. D. E. Rosenfeld, Z. Gengeliczki, B. J. Smith, T. D. P. Stack, M. D. Fayer, Structural dynamics of a catalytic monolayer probed by ultrafast 2D IR vibrational echoes. *Science* **334**, 634–639 (2011).
44. C. L. Anfuso, A. M. Ricks, W. Rodríguez-Córdoba, T. Lian, Ultrafast vibrational relaxation dynamics of a rhenium bipyridyl CO2 -reduction catalyst at a Au electrode surface probed by time-resolved vibrational sum frequency generation spectroscopy. *J. Phys. Chem. C* **116**, 26377–26384 (2012).
45. R. Adato, S. Aksu, H. Altug, Engineering mid-infrared nanoantennas for surface enhanced infrared absorption spectroscopy. *Mater. Today* **18**, 436–446 (2015).
46. X. G. Xu, M. Rang, I. M. Craig, M. B. Raschke, Pushing the sample-size limit of infrared vibrational nanospectroscopy: From monolayer toward single molecule sensitivity. *J. Phys. Chem. Lett.* **3**, 1836–1841 (2012).
47. J. M. Atkin, P. M. Sass, P. E. Teichen, J. D. Eaves, M. B. Raschke, Nanoscale probing of dynamics in local molecular environments. *J. Phys. Chem. Lett.* **6**, 4616–4621 (2015).
48. B. Knoll, F. Keilmann, Near-field probing of vibrational absorption for chemical microscopy. *Nature* **399**, 134–137 (1999).
49. F. Huth *et al.*, Nano-FTIR absorption spectroscopy of molecular fingerprints at 20 nm spatial resolution. *Nano Lett.* **12**, 3973–3978 (2012).
50. E. A. Muller, B. Pollard, M. B. Raschke, Infrared chemical nano-imaging: Accessing structure, coupling, and dynamics on molecular length scales. *J. Phys. Chem. Lett.* **6**, 1275–1284 (2015).
51. R. L. Olmon, P. M. Krenz, A. C. Jones, G. D. Boreman, M. B. Raschke, Near-field imaging of optical antenna modes in the mid-infrared. *Opt. Exp.* **16**, 20295 (2008).
52. O. Krauth, G. Fahsold, N. Magg, A. Pucci, Anomalous infrared transmission of adsorbates on ultrathin metal films: Fano effect near the percolation threshold. *J. Chem. Phys.* **113**, 6330–6333 (2000).
53. M. Litinskaya, F. Herrera, Vacuum-enhanced optical nonlinearities with disordered molecular photoswitches. *Phys. Rev. B* **99**, 041107 (2019).
54. M. Fleischhauer, A. Imamoglu, J. P. Marangos, Electromagnetically induced transparency: Optics in coherent media. *Rev. Mod. Phys.* **77**, 633–673 (2005).
55. R. Fernández-Terán, J. Ruf, P. Hamm, Vibrational couplings in hydridocarbonyl complexes: A 2D-IR perspective. *Inorg. Chem.* **59**, 7721–7726 (2020).
56. A. Moran, S. Mukamel, The origin of vibrational mode couplings in various secondary structural motifs of polypeptides. *Proc. Natl. Acad. Sci. U.S.A.* **101**, 506–510 (2004).
57. J. Langer *et al.*, Present and future of surface-enhanced Raman scattering. *ACS Nano* **14**, 28–117 (2020).
58. N. I. Rubtsova IV, Rubtsov,, Vibrational energy transport in molecules studied by relaxation-assisted two-dimensional infrared spectroscopy. *Annu. Rev. Phys. Chem.* **66**, 717–738 (2015).
59. B. Cohn, A. K. Prasad, L. Chuntonov, Communication: Probing the interaction of infrared antenna arrays and molecular films with ultrafast quantum dynamics. *J. Chem. Phys.* **148**, 131101 (2018).
60. A. B. Grafton *et al.*, Excited-state vibration-polariton transitions and dynamics in nitroprusside. *Nat. Commun.* **12**, 1–9 (2021).
61. J. Keeling, S. Kéna-Cohen, Bose-Einstein condensation of exciton-polaritons in organic microcavities. *Annu. Rev. Phys. Chem.* **71**, 435–459 (2020).
62. F. Herrera, J. Owrutsky, Molecular polaritons for controlling chemistry with quantum optics. *J. Chem. Phys.* **152**, 100902 (2020).
63. K. Nagarajan, A. Thomas, T. W. Ebbesen, Chemistry under vibrational strong coupling. *J. Am. Chem. Soc.* **143**, 16877–16889 (2021).
64. B. Xiang *et al.*, Intermolecular vibrational energy transfer enabled by microcavity strong light-matter coupling. *Science* **368**, 665–667 (2020).
65. A. D. Dunkelberger, B. S. Simpkins, I. Vurgaftman, J. C. Owrutsky, Vibration-cavity polariton chemistry and dynamics. *Annu. Rev. Phys. Chem.* **73**, 429–451 (2022).
66. O. Ávalos-Ovando, L. V. Besteiro, Z. Wang, A. O. Govorov, Temporal plasmonics: Fano and Rabi regimes in the time domain in metal nanostructures. *Nanophotonics* **9**, 3587–3595 (2020).
67. G. Tek, P. Hamm, A correction scheme for Fano line shapes in two-dimensional infrared spectroscopy. *J. Phys. Chem. Lett.* **11**, 6185–6190 (2020).
68. V. Kravtsov, R. Ulbricht, J. M. Atkin, M. B. Raschke, Plasmonic nanofocused four-wave mixing for femtosecond near-field imaging. *Nat. Nanotech.* **11**, 459–464 (2016).
69. J. Nishida *et al.*, Ultrafast infrared nano-imaging of far-from-equilibrium carrier and vibrational dynamics. *Nat. Commun.* **13**, 1–9 (2022).
70. G. Engelhardt, J. Cao, Unusual dynamical properties of disordered polaritons in microcavities. *Phys. Rev. B* **105**, 1–19 (2022).
71. D. Wellnitz, G. Pupillo, J. Schachenmayer, Disorder enhanced vibrational entanglement and dynamics in polaritonic chemistry. *Commun. Phys.* **5**, 120 (2022).
72. S. A. Dönges *et al.*, Multidimensional nano-imaging of structure, coupling, and disorder in molecular materials. *Nano Lett.* **21**, 6463–6470 (2021).
73. R. Wilcken *et al.*, Antenna-coupled infrared nanospectroscopy of intramolecular vibrational interaction. Open Science Frame. https://osf.io/rhnmz/. Deposited 21 April 2023.